STUDY OF TURBULENT DISPERSION OF POLLUTANT PLUMES IN A STAGGERED ARRAY OF OBSTACLES

Bing-Chen Wang
Dept. of Mechanical & Manufacturing Engineering, Univ. of Manitoba
Winnipeg, MB, R3T 5V6, Canada
E-mail: bc_wang@umanitoba.ca

Eugene Yee
Defence Research & Development Canada – Suffield
P.O. Box 4000, Medicine Hat, Alberta, T1A 8K6, Canada
E-mail: eugene.yee@drdc-rddc.gc.ca

Fue-Sang Lien
Dept. of Mechanical & Mechatronics Engineering, Univ. of Waterloo
Waterloo, Ontario, N2L 3G1, Canada
E-mail: fslien@mecheng1.uwaterloo.ca

ABSTRACT

In this research, we report a numerical and experimental study of the turbulent dispersion of a passive scalar released from a continuous ground-level point-source in a staggered array of 16×16 cubic obstacles. The numerical simulation of the flow and scalar fields was based on the Reynolds-averaged Navier-Stokes method and experimental measurements of the flow and dispersion were obtained in a boundary-layer water channel. Results of a detailed comparison between the water-channel experiment of flow and dispersion and model predictions of the mean flow, turbulence kinetic energy, mean concentration and concentration variance are presented.

INTRODUCTION

Turbulent dispersion of passive scalars in an environment with complex geometries represents a challenging topic with vast applications in thermal-fluids engineering, chemical processing, urban atmospheric pollution monitoring, and boundary-layer meteorology. The major challenge associated with this subject involves obtaining a deeper understanding of the interaction of the dynamically evolving flow structures with the complex boundaries, as well as the coupling of the momentum and scalar transport processes.

In order to develop an effective methodology for predicting turbulent dispersion in an urban complex, significant efforts have been made over the past decade based on both experimental and numerical approaches. Recent advances in the study of turbulent dispersion in an urban environment involve a wide range of scales, including field trials conducted at very large regional scales and laboratory simulations conducted in small water channels and wind tunnels. Large-scale urban field studies in the United States have included the Mock Urban Setting Trial (MUST) conducted at U.S. Army Dugway Proving Ground in northwestern Utah in September 2001 (Yee and Biltoft, 2004), the Joint Urban 2003 Experiment conducted in Oklahoma City (Flaherty *et al.*, 2007), and the Urban Dispersion Program (UDP) conducted in New York City over the period from 2004 to 2007 (Allwine *et al.*, 2007). Owing to the need for high-quality data sets for validating numerical models for the prediction of passive scalar dispersion within an urban environment, a number of laboratory studies that measure urban flow and dispersion within idealized building arrays have recently been conducted in wind tunnels (MacDonald *et al.*, 1998; Yee *et al.*, 2006; Pascheke *et al.*, 2008) and water channels (Yee *et al.*, 2006).

The development of numerical models for the concentration variance (second-order moment of concentration) for urban plumes have been undertaken recently, including the work of Andronopoulos *et al.* (2002), Hsieh *et al.* (2007), Milliez and Carissimo (2008), Wang *et al.* (2009) and Yee *et al.* (2009). In the model of Wang *et al.* (2009), the dissipation length scale for concentration variance is determined by the characteristic motions of eddies smaller than the local plume scale in the initial meandering stage of plume development, and is limited by the integral length scale of turbulence when the local plume scale becomes larger than the energy containing eddies of the flow in the turbulent diffusive stage of plume development. In comparison with the model of Wang *et al.* (2009), the model of Yee *et al.* (2009) improves the formulation for the concentration variance dissipation rate by relating it to an inner time scale associated with relative dispersion. To date, this new model of Yee *et al.* (2009) has been validated only against two sets of experimental data on a dispersing plume resulting from a continuous release of a passive tracer within regularly aligned arrays of rectangular obstacles (Wang *et al.*, 2010).

As a further advancement of our previous studies, we report a new set of high-quality water-channel data for turbulent dispersion of a passive scalar released from a localized source in a staggered array of cubic obstacles. In addition, we apply a Reynolds-averaged Navier-Stokes (RANS) method to numerically simulate the physical processes of turbulent dispersion in this staggered array of obstacles, and compare these predicted results with the experimental data reported herein in order to provide further validation of the physically-based model of Yee *et al.* (2009) for the scalar variance dissipation rate.

EXPERIMENTAL MEASUREMENTS

The water-channel simulations of flow and dispersion in staggered obstacle arrays were conducted at Coanda Research & Development Corporation (Burnaby, BC, Canada). The water-channel experiment for various obstacle arrays is fully described in Hilderman and Chong (2007), and only the im-

portant details of the experiment are summarized here. The test section of the water channel is 10 m × 1.5 m × 0.9 m, in the streamwise, spanwise and vertical directions (denoted by x, y and z), respectively. In this paper, we will also use a tensor notation, so these three directions will also correspond to indices 1, 2 and 3, respectively. Fig. 1 shows the staggered array of cubical obstacles in the water channel. This array consists of 16 × 16 cubes, each with a side length $H = 31.75$ mm. The Reynolds number of the flow was approximately $Re_H = 12,005$ (based on H and the free stream velocity $U_b = 0.38$ m s^{-1}).

The velocity field was measured using a 4-beam 2-component TSI fibre-optic laser doppler anemometer (LDA) powered by an argon-ion laser. Titanium dioxide was used as seed particles. The LDA data were collected over a sampling time of 500 s at each position. The data rate for the LDA measurements depended upon the flow velocity, particle seeding density, and optical properties of the lenses, but was typically 50-500 Hz. The measurement volume at the crossing point of the LDA beams ranged in size from 90 μm diameter by 1.3 mm long for the 350 mm focal length lens, to 125 μm diameter by 2.5 mm long for the 500 mm focal length lens.

Detailed measurements were taken at 13 locations in two cells near the centerline of the staggered array of cubes. Fig. 2 exhibits the coordinate system used in the problem definition and Fig. 3 shows the locations for the velocity measurements in the two unit cells. Here, a "cell" represents the basic repeating unit used to construct the obstacle array. A cell of the array occupies an area of $2H \times 2H$ in the x-y plane with the obstacle occupying one (shown shaded in Figs. 2 and 3) of the four quadrants of the cell. Measurements of the vertical profiles of velocity were made in the first (cell 1) and sixth (cell 6) cells in the downstream direction along the eighth column in the array of cubes (i.e., near the centerline of the array).

A 1-D laser induced fluorescence (LIF) linescan system was used for measuring the instantaneous concentration field in the dispersing plume. Sodium fluorescein dye was continuously released from a point source at a rate of 12 ml min^{-1}, and illuminated using a laser beam powered by an argon-ion laser. The dye source was released from a small vertical stainless steel tube (with an inner diameter $d_0 = 2.8$ mm). A Dalsa monochrome digital linescan CCD camera (1024 × 1 pixels), 12-bit (4,096 gray levels) was used to measure the intensity of the dye fluorescence at a sampling rate of 300 Hz for a sampling time of 1,000 seconds at each measurement position. Although a number of ground-level and elevated point-source locations were used in the experiment, we will focus here on only one particular ground-level point-source located midway between rows 1 and 2 along the central column of obstacles (see Figs. 2 and 4 for more details).

NUMERICAL ALGORITHM AND MODELS

The velocity and concentration fields are described by the conservation laws for mass, momentum and concentration for a neutrally-stratified incompressible flow, expressed in the usual ensemble-averaged form. In addition to these conservation laws, the transport equations for turbulence kinetic energy (TKE) k, the rate of dissipation ϵ of TKE and concentration variance $\overline{c'^2}$ are also used. These governing equations assume the following form in a Cartesian coordinate system:

$$\frac{\partial \bar{u}_i}{\partial x_i} = 0, \tag{1}$$

$$\frac{\partial \bar{u}_i}{\partial t} + \frac{\partial (\bar{u}_i \bar{u}_j)}{\partial x_j} = -\frac{\partial \bar{p}}{\partial x_i} + \frac{\partial}{\partial x_j}\left(\nu \frac{\partial \bar{u}_i}{\partial x_j}\right) - \frac{\partial \overline{u'_i u'_j}}{\partial x_j}, \tag{2}$$

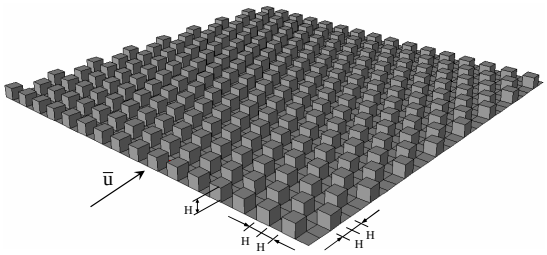

Figure 1: Arrangement of staggered cubic obstacles in the water-channel experiment.

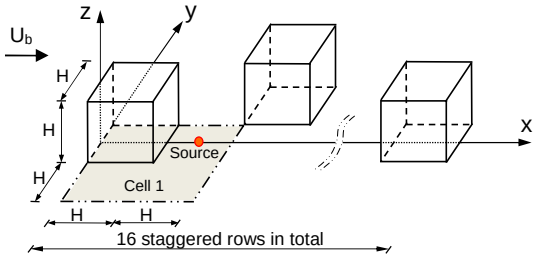

Figure 2: Geometry of the obstacle array in the water channel: central (or, 8th) column of obstacles (with $H = 31.75$ mm).

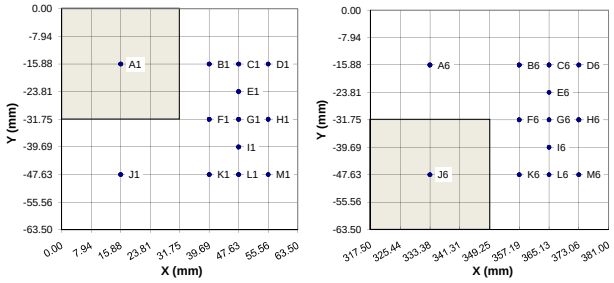

(a) Cell 1 (b) Cell 6

Figure 3: Velocity measurement (or, sampling) locations in cells 1 and 6 (with $H = 31.75$ mm). The x-coordinate in these two subfigures specifies the streamwise location with respect to the coordinate system defined in Fig. 2.

$$\frac{\partial k}{\partial t} + \frac{\partial (\bar{u}_j k)}{\partial x_j} = \frac{\partial}{\partial x_j}\left[\left(\nu + \frac{\nu_t}{\sigma_k}\right)\frac{\partial k}{\partial x_j}\right] + P_k - \epsilon, \tag{3}$$

$$\frac{\partial \epsilon}{\partial t} + \frac{\partial (\bar{u}_j \epsilon)}{\partial x_j} = \frac{\partial}{\partial x_j}\left[\left(\nu + \frac{\nu_t}{\sigma_\epsilon}\right)\frac{\partial \epsilon}{\partial x_j}\right] + \frac{\epsilon}{k}(C_{\epsilon_1} P_k - C_{\epsilon_2}\epsilon), \tag{4}$$

$$\frac{\partial \bar{c}}{\partial t} + \frac{\partial (\bar{u}_j \bar{c})}{\partial x_j} = \frac{\partial}{\partial x_j}\left(D \frac{\partial \bar{c}}{\partial x_j}\right) - \frac{\partial \overline{u'_j c'}}{\partial x_j} + S, \tag{5}$$

$$\frac{\partial \overline{c'^2}}{\partial t} + \frac{\partial (\bar{u}_j \overline{c'^2})}{\partial x_j} = \frac{\partial}{\partial x_j}\left(D \frac{\partial \overline{c'^2}}{\partial x_j} - \overline{u'_j c'^2}\right) - 2\overline{u'_j c'}\frac{\partial \bar{c}}{\partial x_j} - \epsilon_c. \tag{6}$$

Here, $\bar{u}_i$ is the mean velocity in the i-th direction, $\bar{p}$ is the kinematic pressure, $\bar{c}$ is the mean concentration, S is the source density function of the scalar, D is the molecular diffusivity of the scalar, ν is the kinematic viscosity of the fluid, and $\nu_t \stackrel{\text{def}}{=} C_\mu k^2/\epsilon$ is the kinematic eddy viscosity. Eqs. (1)–(4) represent the standard k–ϵ model for the prediction of a turbulent velocity field. The closure constants are given as follows: $C_\mu = 0.09$, $\sigma_k = 1.0$, $C_{\epsilon 1} = 1.44$ and $C_{\epsilon 2} = 1.92$.

The numerical simulations were performed using two in-house computer codes: namely, urbanSTREAM for prediction of the turbulent velocity field and urbanEU for the prediction of the turbulent dispersion of the scalar field. Both codes apply a general curvilinear, second-order accurate, fully conservative and implicit finite-volume method for the discretization of the transport equations for momentum and scalar quantities. The flow solver in urbanSTREAM is based on numerical algorithms described by Lien and

Leschziner (1994). The SIMPLE algorithm was used for the pressure correction. Checkerboard oscillations in the pressure field arising from a state of pressure-velocity decoupling on a collocated grid were removed using a nonlinear momentum interpolation scheme. Detailed descriptions of the algorithms underlying urbanSTREAM and urbanEU can be found in Yee *et al.* (2007).

The computational domain consists of 16 rows and 9 central columns of cubes, with a spatial extent of $61H \times 18H \times 11H$ in the streamwise, spanwise, and vertical directions, respectively. A non-uniform coarse grid of $245 \times 149 \times 48$ control volumes was used for the discretization of the domain. Fig. 4 shows the grid used in our simulations. As shown in Fig. 4, the grid lines have been refined close to the source location and near every solid surface.

At each solid surface, wall boundary conditions were applied for the velocity field (i.e., for the mean velocity and turbulence quantities k and ϵ), and zero-flux boundary conditions were used for the concentration and concentration variance fields. At the inlet, Dirichlet boundary conditions were used for both the mean velocity and concentration fields. The inlet flow conditions for the mean velocity and TKE were obtained from the experimental measurements. The values of concentration and concentration variance at the inlet were set to zero. An upstream fetch of $15H$ (distance between the inlet plane and the windward face of the first row of obstacles) was used in our simulations. For all flow variables, zero-flux boundary conditions were applied at the upper free surface of the computational domain. Neumann boundary conditions were used at the outlet plane, and periodic boundary conditions were applied in the spanwise direction for the velocity field.

Turbulent Stress and Scalar-Flux Models

In order to close the governing equations, the kinematic Reynolds stresses (i.e., $\overline{u_i'u_j'}$) and turbulent fluxes of concentration and concentration variance (i.e., $\overline{u_j'c'}$ and $\overline{u_j'c'^2}$, respectively) need to be modelled. The Reynolds stresses are modelled using the conventional linear eddy-viscosity assumption, from which it follows

$$\overline{u_i'u_j'} = \frac{2}{3}k\delta_{ij} - \nu_t\left(\frac{\partial \bar{u}_i}{\partial x_j} + \frac{\partial \bar{u}_j}{\partial x_i}\right). \tag{7}$$

For the turbulent scalar fluxes, we used the tensor diffusivity model of Yoshizawa (1985), viz.

$$\overline{u_j'c'} = -D_{jk}\frac{\partial \bar{c}}{\partial x_k} \quad \text{and} \quad \overline{u_j'c'^2} = -D_{jk}\frac{\partial \overline{c'^2}}{\partial x_k}, \tag{8}$$

where the tensor diffusivity D_{jk} is defined as

$$D_{jk} = C_{s1}\frac{k^2}{\varepsilon}\delta_{jk} + C_{s2}\frac{k^3}{\varepsilon^2}\left(\frac{\partial \bar{u}_j}{\partial x_k} + \frac{\partial \bar{u}_k}{\partial x_j}\right). \tag{9}$$

Here, $C_{s1} = 0.134$ and $C_{s2} = -0.032$ are two model coefficients.

Concentration Variance Dissipation Model

The critical term in the closure of Eq. (6) is the scalar dissipation: $\epsilon_c \stackrel{\text{def}}{=} 2D\overline{\frac{\partial c'}{\partial x_j}\frac{\partial c'}{\partial x_j}}$. The modelling of ϵ_c determines effectively the rate at which internal concentration fluctuations in the dispersing plume are destroyed by the molecular diffusion. Recently, Yee *et al.* (2009) proposed an advanced modelling for ϵ_c based on the concept of inner-plume time- and length-scales of turbulent diffusion associated with the process of relative dispersion. This model has been previously successfully validated against turbulent dispersion within regularly aligned arrays of rectangular obstacles (Yee *et al.*, 2009; and Wang *et al.* 2010). In this study, we further test this advanced model of Yee *et al.* (2009) against a new

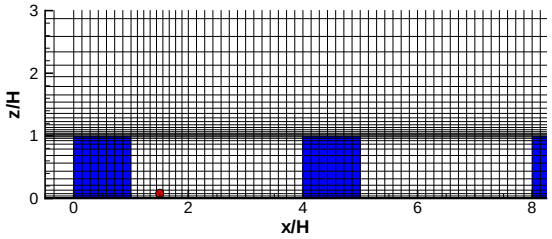

(a) x-z view

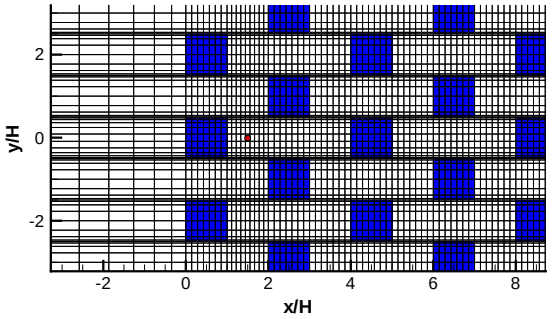

(b) x-y view

Figure 4: Part of the grid system. The red dot indicates the source location.

set of experimental data on turbulent dispersion within a staggered array of obstacles. The model of Yee *et al.* (2009) assumes that:

$$\epsilon_c = c_1\frac{\Delta v(\Lambda_d)}{\Lambda_d}\overline{c'^2}. \tag{10}$$

Here, $c_1 = 1.4$ is a closure constant and $\Delta v(\Lambda_d)$ is the characteristic velocity scale for turbulent eddies whose "size" is Λ_d. The dissipation time scale $t_d \propto \Lambda_d/\Delta v(\Lambda_d)$ corresponds to the eddy turn-over time for eddies that are comparable in size to the mean width of the instantaneous plume, as it is these eddies that are responsible for the in-plume concentration fluctuations and the concomitant scalar dissipation. Here, the characteristic velocity scale is modelled as

$$\Delta v(\Lambda_d) = k^{1/2}\min\left((\Lambda_d/\Lambda_I)^{1/3}, 1\right), \qquad \Lambda_d \geq \sigma_0, \tag{11}$$

where $\Lambda_I \stackrel{\text{def}}{=} k^{3/2}/\epsilon$ is the integral scale of turbulence and σ_0 is the initial source size. The dissipation length scale Λ_d for the concentration variance is determined using the following blending function:

$$\Lambda_d^2 = \frac{l_e^2}{1 + (l_e^2 - \sigma_0^2)/(\sigma_0^2 + c_2 D_t t)}, \tag{12}$$

where $c_2 = 2.7$ is a closure coefficient, t is the travel time, D_t is the turbulent eddy diffusivity, and l_e is the characteristic turbulent eddy size whose growth is determined using the Richardson-Obukhov 4/3-law for relative dispersion.

RESULTS AND ANALYSIS

Before we compare the numerical and experimental results on the velocity and concentration fields in a detailed quantitative manner, it is beneficial to describe qualitatively the general characteristics of these two fields. Fig. 5 displays isopleths of the normalized vorticity magnitude $\Omega \stackrel{\text{def}}{=} (2\bar{\Omega}_{ij}\bar{\Omega}_{ij})^{1/2}/(U_b/H)$ in a partial horizontal plane through the obstacle array at the height $z/H = 0.211$. Here, $\bar{\Omega}_{ij} \stackrel{\text{def}}{=} \frac{1}{2}(\partial\bar{u}_i/\partial x_j - \partial\bar{u}_j/\partial x_i)$ is the resolved mean rotation rate tensor. Fig. 5 provides a qualitative visualization of the complex vortex shedding pattern in the staggered obstacle array predicted using the RANS approach. It is observed that as the flow passes by the cubic obstacles, different types vortical structures are generated. As in the case of the well-known single-cube bluff-body flow case, it is observed that two separation bubbles are formed on both vertical side faces

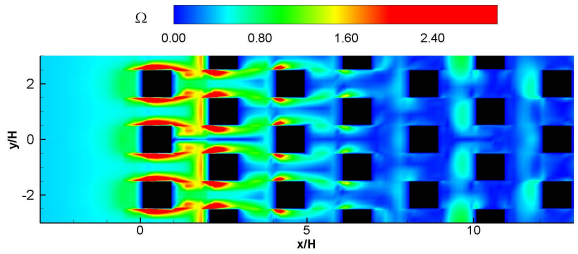

Figure 5: Vortex shedding visualized using the normalized vorticity magnitude $\Omega \stackrel{\text{def}}{=} (2\bar{\Omega}_{ij}\bar{\Omega}_{ij})^{1/2}/(U_b/H)$ (at $z/H = 0.211$).

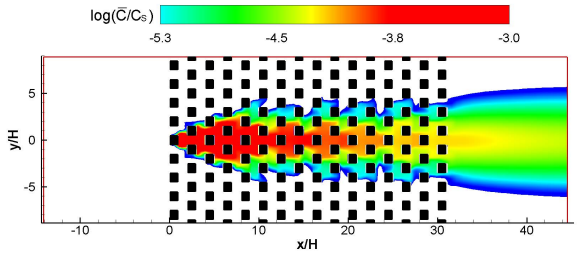

Figure 6: Isopleths of normalized mean concentration field (at $z/H = 0.211$).

of all cubes, as well as a pair of counter-rotating vortices in the wake region on the leeward side of the cubes. These vortical features are the most prominent within the first five rows of the array, although the strength of these vortices is seen to decrease significantly with increasing streamwise distance within the array. Owing to the staggered arrangement of the obstacles, counter-rotating vortices in the wake region of a cube are seen to interact directly with the side face separation bubbles of the two neighbour cubes in the succeeding row immediately downstream of this cube. This represents an interesting dynamic feature in the vortex interaction and evolution in the staggered obstacle array. As is evident from Fig. 5, such wake vortex – separation bubble interactions are the strongest between the first two rows of cubes. From Fig. 5, it is also interesting to observe that owing to the symmetry of the computational domain, there exists a stagnation line in the leeward region of each cube, exactly located along the central streamline of the domain ($y/H = 0$).

Closely related to the special features of vortex dynamics described above, the dispersion of the passive scalar exhibits a very interesting pattern in Fig. 6. In the first 5 rows, the width of the mean plume from the ground-level point-source grows very rapidly in the crosswind (or spanwise) direction. However, in between the 5-th and the 15-th rows, it is seen that the concentration plume exhibits a quasi-periodicity (with a period of 2 rows) in the streamwise direction. This dispersion pattern in the staggered array is in sharp contrast to that shown in the regularly aligned obstacle arrays (Yee *et al.*, 2009; Wang *et al.*, 2009, 2010). In Wang *et al.* (2009, 2010), it has been shown that the flow field (as well as the vortical structures) become quasi-self-similar in the downwind direction after the first several rows and the crosswind plume spread increases monotonically in the streamwise direction. We believe that this interesting streamwise quasi-periodicity pattern in the plume spread observed here is due to complex interactions between the counter-rotating vortices in the wake region of a cube in a row and the side face separation bubbles of the two cubes on both sides of the cube in the succeeding downstream row.

Figs. 7 and 8 compare the predicted mean velocity profiles with two sets of 2-D LDA measurements (i.e., the u-v and u-w configurations) at four locations (see Fig. 3 for the stencil of sampling locations) in cells 1 and 6. The agreement

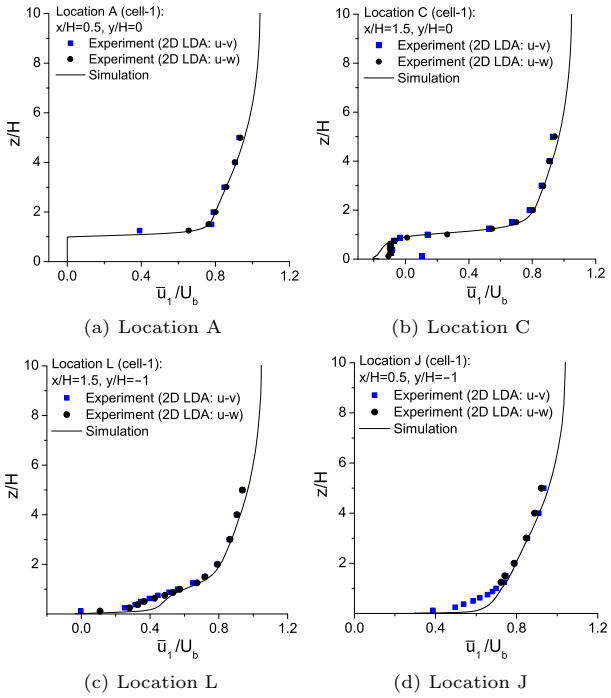

(a) Location A (b) Location C

(c) Location L (d) Location J

Figure 7: Comparison of vertical profiles of the mean velocity at four locations in cell 1.

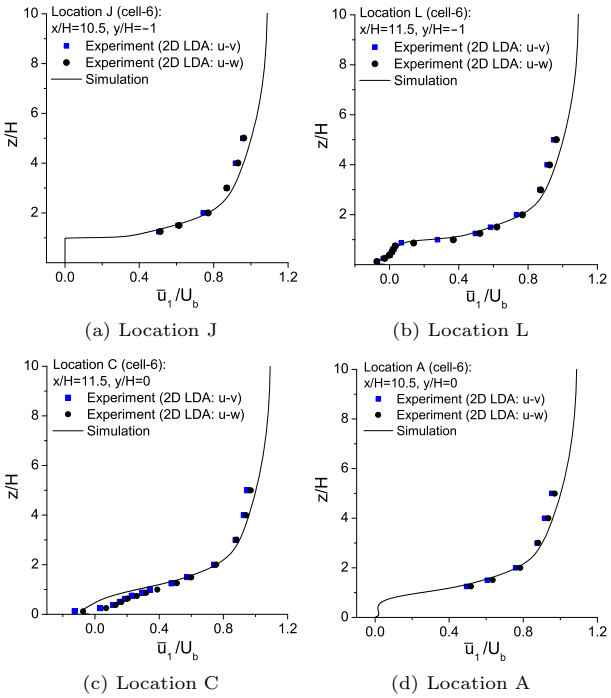

(a) Location J (b) Location L

(c) Location C (d) Location A

Figure 8: Comparison of vertical profiles of the mean velocity at four locations in cell 6.

between the predicted and experimental results is excellent. From Figs. 7(a) and 8(a) , it is observed that the numerical simulations have successfully captured the very strong shear layer near the top of the obstacles (at height $z/H = 1$). Furthermore, as shown in Figs. 7(b), 8(b) and 8(c), the magnitude of the reverse flow ($\bar{u}_1 < 0$) downstream of the leeward face of the obstacle (within the canopy for $z/H < 1$) is correctly reproduced by the simulation. With respect to the stencil of measurement sampling locations, the four locations A, C, L and J in cell 1 correspond geometrically to locations J, L, C and A in cell 6, respectively (see Fig. 3). However, the flow pattern is different between these two

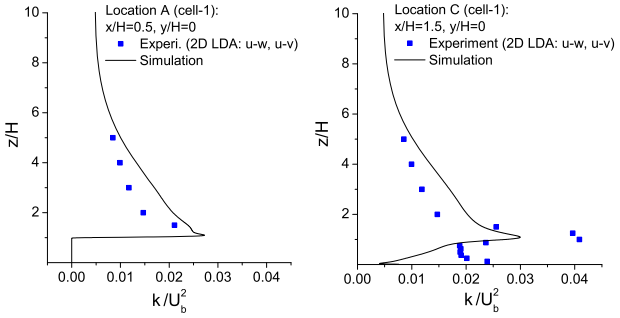

(a) Location A

(b) Location C

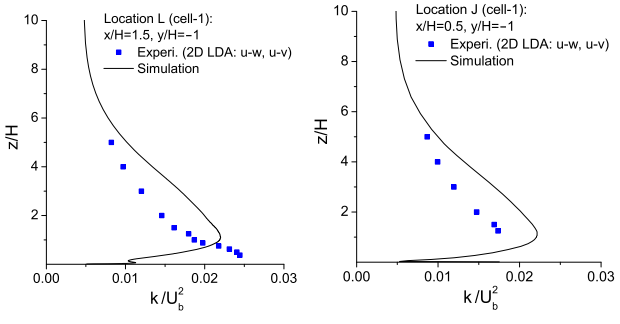

(c) Location L

(d) Location J

Figure 9: Comparison of vertical profiles of the TKE at four locations in cell 1.

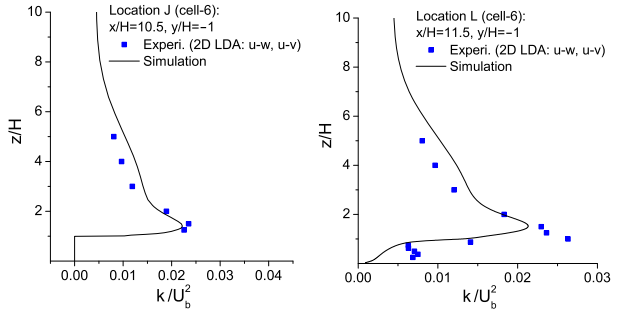

(a) Location J

(b) Location L

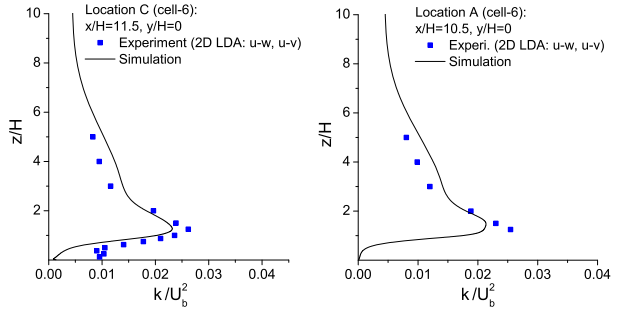

(c) Location C

(d) Location A

Figure 10: Comparison of vertical profiles of the TKE at four locations in cell 6.

cells. By comparing Fig. 7(b) with Fig. 8(b), it is observed that the size of the reverse flow region (or, the recirculation region) is different in these two cells. This is because the inlet flow condition upstream of cells 1 and 6 is different in a sense that cell 6 is, comparatively speaking, more deeply submerged in the internal boundary-layer that is generated over the obstacle array and the flow is much more disturbed due to the cubes upstream of it. There is also a significant difference between the flow patterns shown in Figs. 7(d) and 8(d), although these two sampling locations in cell 1 and 6 are geometrically similar. This difference is expected simply

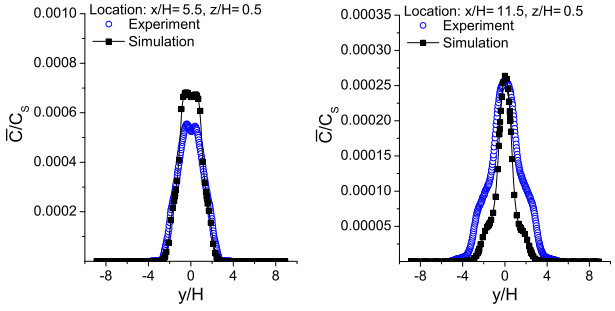

(a) $x/H = 5.5$

(b) $x/H = 11.5$

Figure 11: Mean concentration at half-canopy height ($z/H = 0.5$) at two streamwise locations.

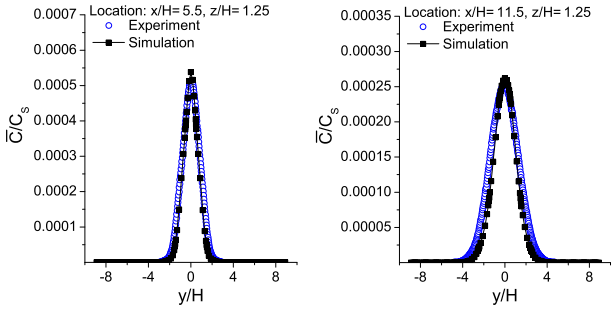

(a) $x/H = 5.5$

(b) $x/H = 11.5$

Figure 12: Mean concentration above the canopy ($z/H = 1.25$) at two streamwise locations.

because there are no cubes upstream of location J in cell 1, as there are of location A in cell 6.

Figs. 9 and 10 show the predicted TKE (k) profiles in comparison with the experimental results in cells 1 and 6. The transport of k is dominated by the vertical spreading of the shear or mixing layer near the top of the canopy ($z/H = 1$), where a large velocity gradient is present (see Figs. 7 and 8). Due to the strong shear production on the top of the obstacles, the TKE level peaks near the top of the canopy. By comparing the numerical results with the water-channel measurement data, it is evident that this physical feature has been correctly reproduced in general by the model predictions. It is especially satisfying to see in Figs. 9(a) and 10(a) that both the vertical location (at or near the top of the canopy) and magnitude of the maximum in the TKE has been correctly reproduced in the simulations.

Figs. 11 and 12 compare predictions and measurements of the mean concentration at two fixed sampling locations downwind of the source (i.e., $x/H = 5.5$ and $x/H = 11.5$, respectively) at half-canopy height ($z/H = 0.5$) and above the canopy ($z/H = 1.25$), respectively. It is seen from the figures that the shapes of the mean concentration profiles are correctly predicted by the model. By comparing Fig. 11(a) with Fig. 12(a), it is observed that the crosswind mean concentration profile below the canopy top tends to be non-Gaussian (and, more specifically, is seen to exhibit a bimodal form due to the bifurcation of the plume as it sweeps around the sides of an obstacle). However, the crosswind profile of the mean concentration above the canopy tends to be Gaussian. The bifurcation of the concentration surrounding the cubes relates to the divergence of the flow around an obstacle shown in Fig. 5, and the effect of this flow divergence on dispersion is the strongest within the canopy and diminishes quickly in the region above the canopy as the elevation from the top surface of the obstacles increases. Figs. 13 and 14 compare the standard deviation of concentration $(\overline{c'^2})^{1/2}$ [or, root-mean-square (RMS) concentration], at the same measurement locations for the mean concentra-

tion. From Figs. 13 and 14, it is observed that the numerical predictions of $(\overline{c'^2})^{1/2}$ are in quite good conformance with the measurements.

CONCLUSIONS

The continuous release of a passive tracer from a ground-level point-source in a staggered array consisting of 16×16 cubic obstacles has been studied using both the numerical and experimental methods. The numerical simulation is based on a RANS model which uses the standard eddy viscosity closure model for the Reynolds stresses, the tensor-diffusivity closure model of Yoshizawa (1985) for the scalar-fluxes, and a recent model of Yee *et al.* (2009) for the concentration variance dissipation rate. In comparison with the 2-D LDA and 1-D LIF measurements conducted in the water channel, the RANS-based simulation predicted successfully the highly disturbed mean velocity, the turbulence kinetic energy, the mean concentration and concentration variance both within and above the obstacles. The strong shear rate and shear production near the top of the canopy have been correctly captured by the model predictions.

Owing to the direct interaction between the counter-rotating vortices in the wake region of a cube in a row and the separation bubbles on the side faces of the two neighboring cubes in the immediate successive downstream row, the crosswind profile of the mean concentration exhibits a quasi-periodicity in the streamwise direction with a period of 2 rows. These special vortex dynamics and passive scalar dispersion patterns are unique to the staggered obstacle array, and are distinctively different from those similar observations in regularly aligned arrays of obstacles (Yee *et al.*, 2009; Wang *et al.*, 2009, 2010).

Conceptually, the concentration variance dissipation rate model of Yee *et al.* (2009) is very attractive since it embodies the basic physics of in-plume concentration fluctuations related to relative dispersion that are responsible for turbulent mixing and dissipation. This model of Yee *et al.* (2009) has been previously validated based on cases of flow and dispersion in regularly aligned obstacles (Yee *et al.*, 2009; Wang *et al.*, 2010). In this paper, we further confirm the good performance of this relatively new model by testing it against a new set of high-quality water-channel measurement data on dispersion in a staggered array of cubes.

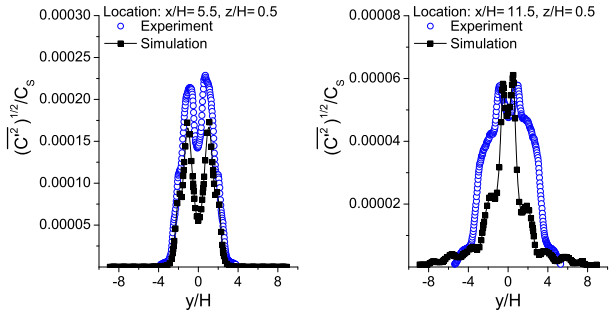

(a) $x/H = 5.5$ (b) $x/H = 11.5$

Figure 13: Standard deviation of the concentration at half-canopy height ($z/H = 0.5$) at two streamwise locations.

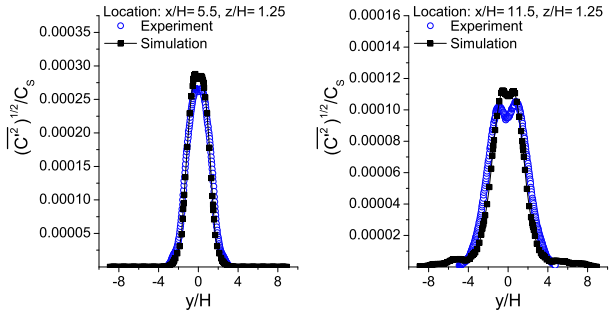

(a) $x/H = 5.5$ (b) $x/H = 11.5$

Figure 14: Standard deviation of the concentration above the canopy ($z/H = 1.25$) at two streamwise locations.

REFERENCES

Allwine, K. J., Clawson, K. L., Flaherty, J. E., Heiser, J. H., Hosker, R. P., Leach, M. J., and Stockham, L. W. (2007), "Urban dispersion program: Urban measurements applied to emergency response", in *Proceedings of the Seventh Symposium on the Urban Environment*, American Meteorological Society, San Diego, California, 5 pages.

Flaherty, J. E., Lamb, B., Allwine, K. J., and Allwine, E. (2007), "Vertical tracer concentration profiles measured during the Joint Urban 2003 dispersion study", *J. Appl. Meteorol. Climatol.*, vol. 46, pp. 2019–2037.

Hilderman, T. and Chong, R. (2007), "A laboratory study of momentum and passive scalar transport and diffusion within and above a model urban canopy — final report", *Technical Report: DRDC Suffield CR 2008-025*, Defence R&D Canada – Suffield, Ralston, Alberta, 78 pages.

Hsieh, K. J., Lien, F.-S., and Yee, E. (2007), "Numerical modeling of passive scalar dispersion in an urban canopy layer", *J. Wind Eng. Ind. Aerodyn.*, vol. 95, pp. 1611–1636.

Lien, F.-S. and Leschziner, M. A. (1994), "A general non-orthogonal collocated finite volume algorithm for turbulent flow at all speeds incorporating second-moment turbulence-transport closure, Part 1: computational implementation", *Comput. Meth. Appl. Mech. Eng.*, vol. 114, pp. 123–148.

MacDonald, R. W., Griffiths, R. F., and Hall, D. J. (1998), "A comparison of results from scaled field and wind tunnel modelling of dispersion in arrays of obstacles", *Atmos. Environ.*, vol. 32, pp. 3845–3862.

Milliez, M. and Carissimo, B. (2008), "Computational fluid dynamical modelling of concentration fluctuations in an idealized urban area", *Boundary-Layer Meteorol.*, vol. 127, pp. 241–259.

Pascheke, F., Barlow, J. F., and Robins, A. (2008), "Wind-tunnel modelling of dispersion from a scalar area source in urban-like roughness", *Boundary-Layer Meteorol.*, vol. 126, pp. 103–124.

Yee, E. and Biltoft, C. A. (2004), "Concentration fluctuation measurements in a plume dispersing through a regular array of obstacles", *Boundary-Layer Meteorol.*, vol. 111, pp. 363–415.

Yee, E., Gailis, R. M., Hill, A., Hilderman, T., and Kiel, D. (2006), "Comparison of wind-tunnel and water-channel simulations of plume dispersion through a large array of obstacles with a scaled field experiment", *Boundary-Layer Meteorol.*, vol. 121, pp. 389–432.

Yee, E., Wang, B.-C., and Lien, F.-S. (2009), "Probabilistic model for concentration fluctuations in compact-source plumes in an urban environment", *Boundary-Layer Meteorol.*, vol. 130, pp. 169–208.

Yoshizawa, A. (1985), "Statistical analysis of the anisotropy of scalar diffusion in turbulent shear flows", *Phys. Fluids*, vol. 28, pp. 3226–3231.

Wang, B.-C., Yee, E., and Lien, F.-S. (2009), "Numerical study of dispersing pollutant clouds in a built-up environment", *Int. J. Heat Fluid Flow*, vol. 30, pp. 3–19.

Wang, B.-C., Yee, E., and Lien, F.-S. (2010), "Prediction of second-order concentration statistics for dispersing plumes in obstacle arrays", *Prog. Comput. Fluid Dyn.*, vol. 10, pp. 252–262.